ELECTRONIC SUPPLEMENTARY INFORMATION

Real-Time Observation of Self-Limiting SiO_2/Si Decomposition Catalysed by Gold Silicide Droplets

Petr Bábor[†‡], Radek Duda[†‡], Josef Polčák[†‡], Stanislav Průša[†‡], Michal Potoček[†‡], Peter Varga[†], Jan Čechal[†‡], Tomáš Šikola[†‡]*

[†]CEITEC - Central European Institute of Technology, Brno University of Technology, Technická 3058/10, 616 00 Brno, Czech Republic.

[‡]Institute of Physical Engineering, Brno University of Technology, Technická 2896/2, 616 69 Brno, Czech Republic.

CONTENTS:

1. Electron beam induced SiO_2 decomposition

The ability of the e-beam to locally decompose a 10 nm SiO_2 layer is demonstrated in Figure S1. The e-beam was scanned over the small area (45×190 nm^2; marked by the yellow arrow) for 5.5 seconds; this led to a nearly complete decomposition of the whole thickness of the SiO_2 layer within the exposed area. On the other hand, no apparent changes in oxide layer thickness were observed when a large area was imaged. Figure S1d,e documents that there is no observable influence of electron beam exposure on the propagation rate of the void rim during both thermal (bottom void) and Au NP assisted (upper void) oxide decomposition.

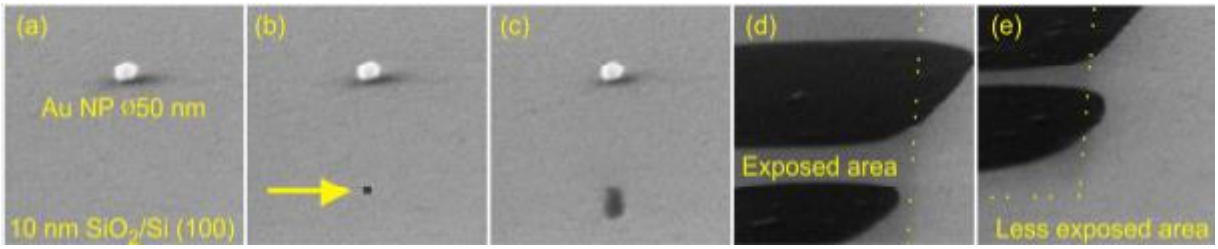

Figure S1. The sequence of the selected SEM micrographs (frames) measured at a constant temperature (~750 °C) demonstrating the ability of e-beam to decompose SiO_2. (a) Au sphere (diameter of 50 nm) on SiO_2 (thickness of 10 nm) deposited on a Si(001) substrate. (b) Small rectangular spot (highlighted by the yellow arrow) is formed at the position of the e-beam held there for 5.5 seconds. (c) Subsequently, the void starts to grow via a standard oxide decomposition mechanism. (d, e) SEM images showing the areas exposed both by high (real-time observed for prolonged period of time) and very low electron dose (only the last image). The border between these areas is marked by the dotted yellow line. The same oxide decomposition rate is observed for both areas. The sequence of images is taken from the supplementary movie SM-2.

2. Role of the electron beam on Au catalysed SiO_2 decomposition

Because the electron beam is only lowering the activation energy of oxide decomposition by inducing preferential oxygen desorption[S1] it should have no effect on the release of Si atoms from surface and its diffusive transport. Hence, we can exclude the role of electron beam on the processes (1) and (2). Our observations show that the electron beam irradiation decreases the temperature for the void nucleation by a described mechanism only if view-field is zoomed to small areas and high electron beam intensity is used. No effects are observed when the large view-fields and low beam intensities are employed. The negligible effect on the steps (3) and (4) is corroborated by the observed constant growth rate of the void size regardless its local illumination by the electron beam. More specifically, (i) when we zoomed into particular part of propagating void rim its propagation rate did not change – after zooming out we found that all the parts of the rim moved by the same distance and (ii) when the AuSi droplet wetting the void rim was depleted the void growth rate decreased or was terminated even when the surface was irradiated by the electron beam (see Section 1 of SI).

3. Chemical analysis of a gold layer by ToF-LEIS and XPS

Additional experiments were carried out in a home-built complex ultra-high vacuum (UHV) system.[S2] The employed experimental methods – Time of Flight Low Energy Ion Scattering (ToF-LEIS) and X-ray Photoelectron Spectroscopy (XPS) – provide area averaged information on the sample near-surface composition. Hence, one should be careful when interpreting them in context of local information provided by SEM. However, in the final stage of oxide decomposition all the gold is present in the form of a AuSi monolayer covering the bare Si surface. Therefore, ToF-LEIS and XPS can be used to determine the properties of this monolayer.

For these experiments, the substrates were cut from a Si(001) wafer (ON Semiconductor, phosphorus doped, resistivity 0.0089 – 0.0093 cm) with a native silicon oxide layer on top. First, the native oxide layer was removed by immersing it in 1 M HF solution for 120 s. Afterwards the substrate was rinsed in deionized water and subsequently immersed in a colloidal solution of 10 nm Au NPs in water buffered with 3 mM of HF acid for one hour.[S3] During this step silicon substrate is re-oxidized and a thin chemical silicon oxide layer formed. The oxide thickness was 0.6 nm as determined by XPS analysis.[S4] The use of the thinner oxide enables us to reduce the void nucleation temperature whereas the mechanism of oxide decomposition remains unchanged.[S5-S7]

The Au NP covered sample was introduced to UHV system and annealed by PBN heater from room temperature up to ~800 °C with a temperature ramp of 36 °C/hour. The temperature was determined from the current passing through the PBN heater using a previously measured calibration curve obtained by a K-type thermocouple attached directly to the Si sample surface; the estimated error of temperature determination was ±15°C. During the annealing the pressure was below $6 \cdot 10^{-6}$ Pa. LEIS and XPS spectra were acquired during annealing while the sample was at a specific temperature.

ToF-LEIS analysis was carried out by a home-made spectrometer[S8, S9] using 5 keV He^+ ions impinging (current 1.5 nA) the sample surface in the normal direction; the scattering angle was 152° and the size of analysed area was 4 mm^2. Scattered particles were detected by a triple Hammamatsu F-2221-31S detector at the end of 1.23 m long drift tube equipped with acceleration electrodes used for separation of scattered ions and neutrals.

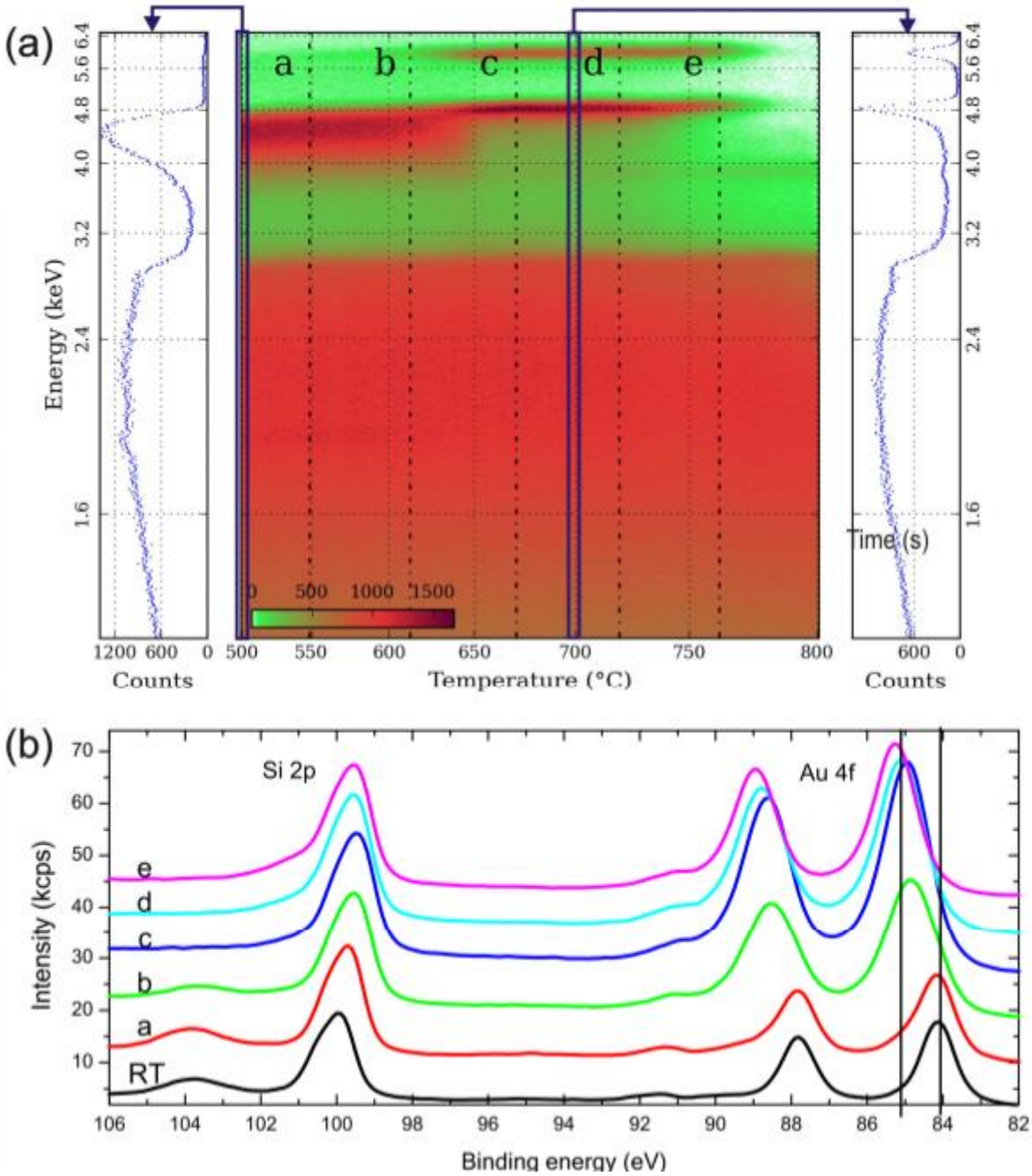

Figure S2. (a). Evolution of ToF-LEIS spectra during thermal annealing displayed as 2D map: for the specific temperature the spectrum is presented as a line with colour coding the intensity. The initial spectrum is shown at the left side and the spectrum at the right was taken at 700 °C. (b) XPS spectra taken at a different sample prepared in the same way as for ToF-LEIS one. The labels "a" to "e" refers to the temperatures marked by vertical lines in ToF-LEIS spectra.

X-ray Photoelectron Spectroscopy (XPS) analysis was carried out in-situ in a separate chamber using the Omicron DAR400 X-ray source and EA125 electron energy spectrometer. All measurements were done in the constant analyser energy (CAE) mode using Al K radiation; pass energy of 25 eV; and emission angle of 50 ° (according to the surface normal direction).

LEIS spectra acquired during the sample annealing are presented in Figure S2a in form of a 2D map. At room temperature (spectrum on the left side) there are two dominant contributions: (1) a broad peak centred at 4.4 keV associated with scattering of He ions at Au atoms ($He^+ \rightarrow Au \rightarrow He^0$) and (2) intensity increase for energies below 3.1 keV related to He^+ scattering at SiO_2/Si substrate. At temperatures 620 – 650 °C the peak at 4.4 eV decreases and transforms into two narrow peaks at energy of 4.6 keV ($He^+ \rightarrow Au \rightarrow He^0$) and 5.8 keV ($He^+ \rightarrow Au \rightarrow He^+$), respectively. As He neutrals scattered from deeper regions lose more energy as a result of multiple scattering events and inelastic losses during their penetration through the material, the FWHM of the peaks in the LEIS spectra increases approx. linearly with the thickness of analyzed layers, only He neutrals scattered at the Au atoms localized at the surface have a maximal scattering energy of 4632 eV. The peak at 5.8 keV ($He^+ \rightarrow Au \rightarrow He^+$) originates due to the scattering of He ions at surface Au atoms when the He ions retain their charge; energy of these ions is shifted by a post acceleration before the detection. Hence, both peaks are associated with Au surface atoms.

During the transformation the FWHM of the ($He^+ \rightarrow Au \rightarrow He^0$) peak decreases almost 3 times. If we consider the initial diameter of nanospheres 10 nm, the thickness during the transformation should decrease below 3 nm. This value is, however, the same as the depth resolution of the TOF-LEIS analyzer and, hence, the resulting thickness can be lower. The presence of the second narrow peak at 5.8 keV ($He^+ \rightarrow Au \rightarrow He^+$) being associated only with atoms in the topmost layer confirms that the layer should be very thin.[S10] The XPS analysis (Figure S2b) shows that the oxide film remains intact up to ~620 °C. Within this temperature region the Au $4f_{7/2}$ peak is at the position of pure bulk gold.[S11] Beyond this temperature the thin oxide layer is decomposed and the Au 4f peak shifts by 1.2 eV towards higher binding energies and increases in intensity by factor of 3 suggesting the transformation of Au into AuSi[S10] and lateral spreading of Au atoms. These observations are consistent with the formation of a monolayer thick Au layer emerging after the oxide decomposition.

4. Morphological analysis of void by AFM

Figure S3 presents the topographic image of the void measured by AFM after sample cooling in the SEM microscope and its exposing to ambient conditions. The same sample used for real time measurements – Si(001) with a 10 nm thermal SiO_2 layer covered with 80 nm Au NPs – was used also for subsequent AFM measurements. The sample was first annealed at 730 °C and the formation of voids was observed by SEM. When the particular void was nucleated the heating was turned off and sample cooled. After the venting of the SEM, the particular void was localized and measured by AFM in the atmosphere within 20 minutes.

The overall shape of the void shown in Figure S4 agrees with the SEM observation and its bowl-like morphology with the one recently discussed by Hibino *et al* for uncatalysed growth.[S7] The multiple protrusions in the void including the central one were formed during the sample cooling.

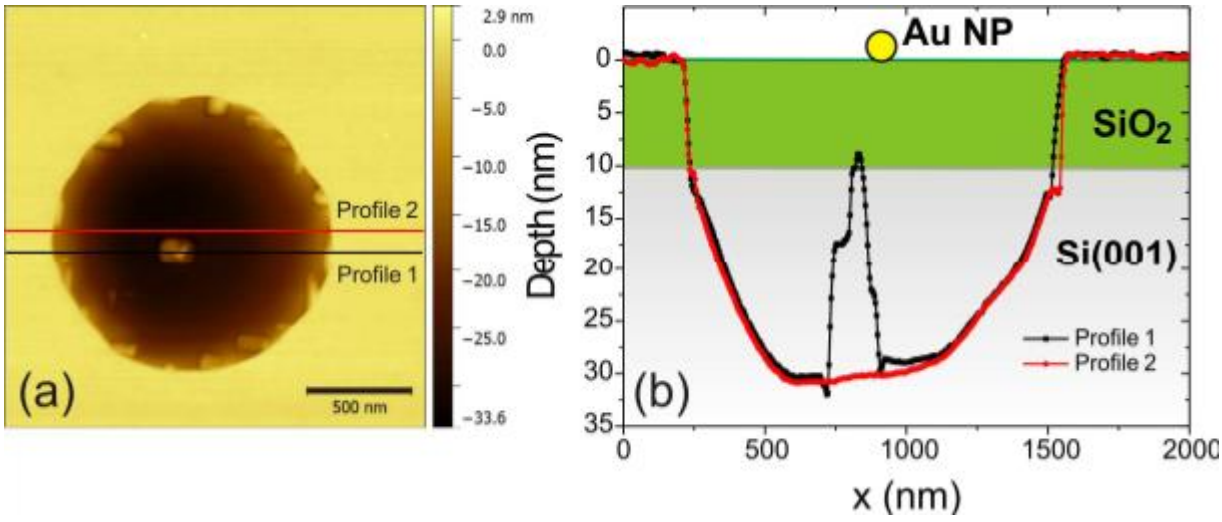

Figure S3. (a) AFM micrograph of the void nucleated at the position of the Au NP and grown during sample annealing at the temperature of 730 °C. (b) AFM profiles 1 and 2 associated with marked red and black lines in the AFM image. The initial sample morphology the 10 nm thick silicon oxide layer in green and the original position of the Au NP is highlighted by yellow circle.

5. Resuming SiO_2 etching when supplied by Au NPs

Figure S4 shows the formation and growth of two voids marked as V_A, V_B near a large void V_C already depleted of Au. Initially, the rim of both voids propagates with velocity of 3 nm/s until 182 s. When the propagating rim of V_A reaches a Au NP, the nanoparticle quickly transforms into the AuSi droplet and Au atoms spread across the bare silicon surface inside the void, which is observable by change of contrast of V_A to a brighter one compared with V_B at 194 s. Consequently, the velocity of the void rim increases to 50 nm/s. When the rim of the V_A comes into contact with the rim of V_B, the bare surface of V_B is quickly filled by Au atoms (196 s) and the velocity of V_B rim increases also to 50 nm/s. The both voids grow with the high rate until they merge with the rim of V_C. The excess Au atoms from V_A and V_B spread in V_C and consequently the voids V_A and V_B become depleted of Au atoms and their velocity decreases to 3 nm/s.

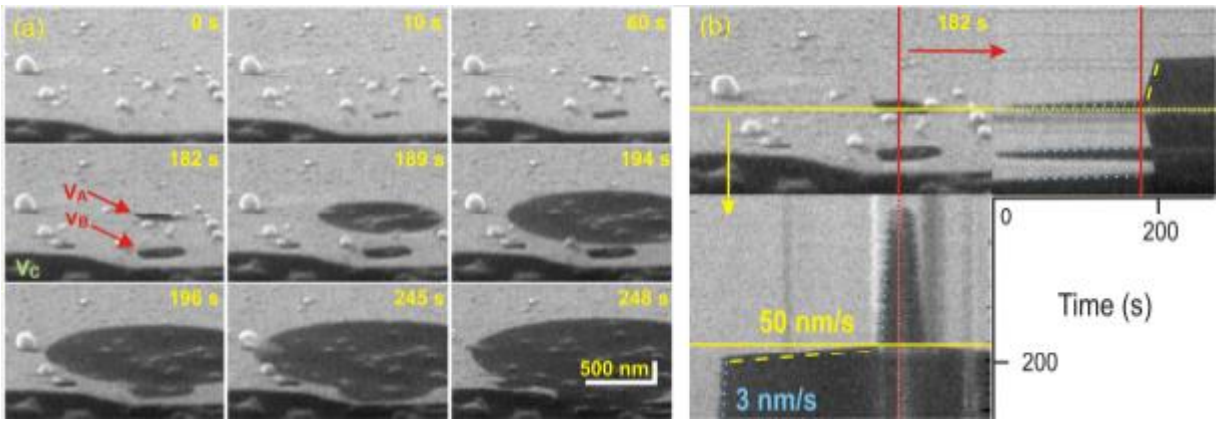

Figure S4. (a). The sequence of the SEM micrographs (frames) of Au spheres with different sizes on a 10 nm SiO_2/Si(001) substrate at constant temperature (~700 °C). Two voids V_A and V_B nucleate near the large void V_C. (b) The sequence of horizontally compressed cuts of the void V_A as a function of time. The position of the cuts is marked by the yellow and red lines. The fast and slow propagation of the void rim is highlighted by the dashed yellow and dotted blue lines, respectively. For the full sequence see Supplementary Movie SM-3.

6. References

S1 H. Watanabe, S. Fujita, S. Maruno, K. Fujita, M. Ichikawa, *Appl. Phys. Lett.* 1997, **71**, 1038.

S2 S. Voborny, M. Kolibal, J. Mach, J. Cechal, P. Babor, S. Prusa, J. Spousta, T. Sikola, *Thin Solid Films* 2004, **459**, 17.

S3 M. Kolibal, M. Konecny, F. Ligmajer, D. Skoda, T. Vystavel, J. Zlamal, P. Varga, T. Sikola, *ACS Nano* 2012, **6**, 10098.

S4 M.P. Seah,; S. J. Spencer, *Surf. Interface Anal.* 2002, **33**, 640.

S5 Y. Wei, R. M. Wallace, A. C. Seabaugh, *Appl. Phys. Lett.* 1996, **69**, 1270.

S6 N. Miyata, H. Watanabe, M. Ichikawa, *Phys. Rev. Lett.* 2000, **84**, 1043.

S7 H. Hibino, M. Uematsu, Y. Watanabe, *J. Appl. Phys.* 2006, **100**, 113519.

S8 M. Kolibal, O. Tomanec, S. Prusa, M. Plojhar, S. N. Markin, L. Dittrichova, J. Spousta, P. Bauer, T. Sikola, *Nucl. Instrum. Methods Phys. Res., Sect. B* 2007, **265**, 569.

S9 P. Babor, R. Duda, S. Prusa, T. Matlocha, M. Kolibal, J. Cechal, M. Urbanek, T. Sikola, *Nucl. Instrum. Methods Phys. Res., Sect. B* 2011, **269**, 369.

S10 D. Goebl, B. Bruckner, D. Roth, C. Ahamer, P. Bauer, *Nucl. Instrum. Methods Phys. Res., Sect. B* 2015, **354**, 3.

S10 J. Cechal, J. Polcak, T. Sikola, J. *Phys. Chem. C* 2014, **118**, 17549.